Development of a 200 mg bio-inspired nano-flying robot

T. Jardin*, S. Prothin, P. Barricau and J.R. Frutos
ISAE-SUPAERO, Université de Toulouse, France
SilMach, Besançon, France

Abstract

We report on the development of a 200 mg flapping wing robot. The flapping motion is driven by a simple rod-crank system connected to an electrostatic motor operating at frequencies up to a few Hertz. The wings are connected to the rod-crank system via a few tens of μm thick hinge which allows passive wing rotation at stroke reversal. Components of the robot are manufactured out of silicon, Titane, PEEK and Parylene to reduce weight and friction. A test bench is developped that allows to reproduce the wing dynamics of the 200 mg prototype, with enhanced robustness and larger range of operating frequency. Three systems with 60, 90 and 120° flapping amplitudes and interchangeable wings operating at frequencies up to 30 Hertz are used for long lasting experiments. The dynamics of the wings are analyzed using High Speed Camera Visualization (HSV) and aerodynamic loads are derived from Particle Image Velocimetry (PIV) measurements in the wake of the robot and compared with balance measurements. Kinematics of the wings obtained from HSV are then implemented to extract forces and 3D velocity flow fields from Direct Numerical Simulations (DNS). Results show that for high frequencies and flapping amplitudes, the robot is able to produce lift up to 600 mg. For these specific cases, it can be observed from HSV that aerodynamic and inertial forces are sufficient for the wing to bend chordwise (around the hinge) and operate at angles of attack close to 45°. Chordwise bending decreases as the flapping frequency decreases resulting in a frequency threshold below which no lift is being generated. In addition, results show that loads derived from PIV match those obtained from balance measurements and can therefore be used to measure even lower lift production where balance measurements are not accurate. Finally, DNS helps reveal prominent aerodynamic mechanisms at play.

*Email address(es): thierry.jardin@isae.fr

1 Introduction

The recent advent of micro and nano-technologies have paved the way for the development of extremely small-sized robots capable of flying in confined environments. At these scales, typically on the order of the centimeter, aerodynamic performance of conventional rotary wing concepts drastically decreases due to increased flow viscous effects with respect to inertial effects, i.e. due to extremely-low-Reynolds-number effects. Consequently, because nano-flying robots operate on the same scale of insects, the flapping wing concept has long been proposed as a prospective alternative to the conventional rotary wing concept [1]. However, despite extensive researches over these two or three past decades, there is no compelling evidence that flapping wings are more aerodynamically efficient than rotary wings, even at very low Reynolds numbers. This lack of evidence can partly be explained by our inability to optimize flapping kinematics due to the very large parameter space that needs to be explored. Similarly, while some studies indicate that flapping wings may produce larger lift than rotary wings, there is no compelling evidence that this is intrinsically valid since comparisons are usually performed under restrictive asumptions (e.g. at same operating frequency). Further investigations on flapping wings should thus be conducted to clarify the picture. Yet, apart from pure aerodynamic considerations, [2] suggested that flapping wing concepts could be more efficient than rotary wing concepts at very small scale (fruit fly scale) when taking into account the actuator performance (oscillatory versus rotary). In addition, flapping wings could potentially be conducive to both enhanced maneuverability and aero-acoustic stealth.

In this context, we report on the development of a 200 mg bio-inspired, flapping wing robot. The flapping motion of the wings is driven by a continuous electrostatic motor connected to a simple rod-crank system. The pitching motion (about the wing's leading edge) is passive and results from the dynamic response of the wing structure to aerodynamic and inertial forces. Wings with different structures are manufactured and tested on three different configurations of the rod-crank system with flapping amplitudes 60, 90 and 120°. The aerodynamic lift generated by the flapping wings is assessed for flapping frequencies up to 30 Hz using both balance and particle image velocimetry (PIV) measurements. High-speed camera visualizations are used to extract wing motion and deformation (i.e. flapping, passive pitch and spanwise bending) during the flapping cycle, which is then used for direct numerical simulations (DNS) of the flow past the flapping wings.

Overall, this study shows that the present robot can gener-

ate lift about three times its target weight when operated at the largest flapping amplitudes and frequencies and with a wing structure that allows for sufficient pitch amplitude. In addition, it is shown that lift obtained from both balance and PIV measurements match within reasonable accuracy, suggesting that PIV measurements could be used for lift evaluation at even lower scales, i.e. where balances are not accurate. Lift obtained from numerical simulations also reasonably agrees with experimental data, which allows to correlate prominent flow features with aerodynamic performance.

2 Materials and Methods

The flapping robot consists of two wings connected to an electrostatic motor via a rod-crank system. The wings are manufactured out of Titane TA6V (chemical cutting procees for structure) and Parylene (chemical vapor deposition method for the membrane). They weight approxiamtely 10 mg with chord and span dimensions of approximately 1 and 3 cm respectively. A 25 μm thick hinge allows the main part of the wing to passively pitch (about its leading edge) with respect to a second part that is rigidly fixed to the rod-crank system. The electrostatic motor is manufactured out of silicon (SilMach's PowerMEMS patented solution). It weights less than 40 mg and is able to operate at frequencies up to a few Hertz. For experimental tests described below, the motor is replaced by a Faulhauber commercial brushless DC-Servomotor (5g weight) to allow operating frequencies up to 30 Hz (figure 1). Finally, the rod-crank system is manufactured out of Titane TA6V and PEEK to minimize both mass and friction, for a weight below 70 mg. For testing purposes, three different rod-crank arrangements are considered, yielding flapping amplitudes of 60, 90 and 120°. The final weight of the protoype is approximately 200 mg.

2.1 Load measurements

The lift produced by the flapping wings is first measured using a Kern EMR 1000-2 balance with a precision of 10 mg and a maximum range of 1000 g. The robot is mounted upside-down on a 3D-printed support to avoid any bias resulting from ground effects (i.e. interaction between the wake of the flapping wings and the ground), see figure 1. The balance provides a steady value for lift. In what follows, reported values for lift are obtained by averaging ten consecutive measurements. Error bars are derived from the maximum deviation of each measurement to the averaged value, corresponding to an uncertainty of ± 20 mg.

2.2 PIV measurements

In addition to direct load measurements from balance, stereoscopic particle image velocimetry (PIV) measurements in the wake of the robot are performed (figure 2) to indirectly extract forces from flow velocity integration on a control volume.

The environing fluid is seeded with oil particles. A Nd:YAG laser illuminates particles in a 3 mm thick sheet located 40 mm below the robot. Two high-definition FlowSense EO 16M cameras (4872 px $\times$ 3248 px resolution) synchronized with the laser acquire double-framed images of particles in the laser sheet at a frequency of approximately 2 Hz using Dantec DynamicStudio . The time step between two frames depends on the operating frequency of the robot (which is related to the wake velocity) and is on the order of a few tens of μs. It is chosen to ensure that enough particles remain within the 3 mm thick laser sheet between two frames. The angle between the laser sheet and the cameras is close to 45° to maximize measurement accuracy on both in-plane and out-of-plane displacements.

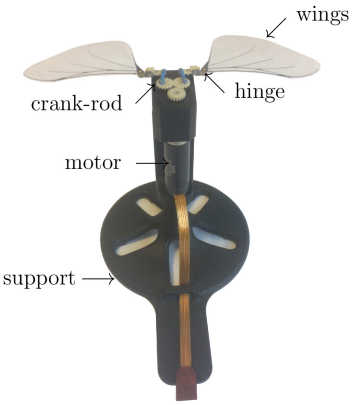

Figure 1: The nano-flying robot mounted (upside down) on the balance support.

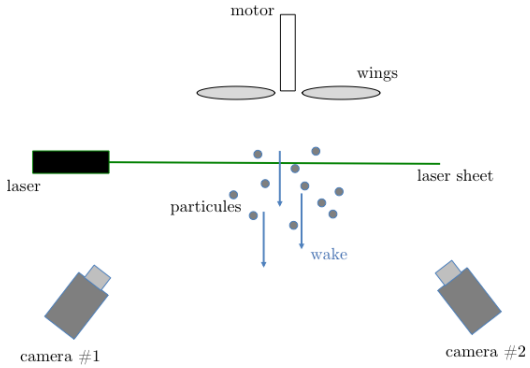

Figure 2: Scheme of the experimental setup for PIV measurements.

After removing background noise, two frames are cross-correlated to obtain an instantaneous, two-component pixel displacement field for each image of each camera. Multi-pass cross-correlation is performed using interrogation windows with decreasing size, from 64$\times$64 to 16$\times$16 pixel square.

Corresponding instantaneous pixel displacement fields from the two cameras are then used to reconstruct a two-

dimensional, three-component displacement field. Velocity fields are deduced from displacement fields knowing the time step between two frames.

For each case, 500 instantaneous velocity fields are averaged to obtain a mean (statistically converged) flow field which is then used to extract lift from velocity integration.

2.3 Load extraction from PIV

Instantaneous aerodynamic forces experienced by a body can be extracted by integrating momentum equations on a control volume enclosing the body [3, 4]. This typically requires knowledge of acceleration flow fields inside the control volume and velocity and pressure fields on control surfaces. While time-resolved volumetric PIV measurements can provide such data, it remains highly challenging and restricted to some specific cases. When mean aerodynamic forces are considered, the approach reduces to the integration of velocity and pressure forces on control surfaces [5]. In addition, if the control surfaces are suffciently far away from the body, the sole integration of the velocity field in the wake of the body can provide reasonable estimates of the mean force perpendicular to the measurement plane. Hence, the lift generated by the robot is here derived from integration of the mean vertical velocity field in the PIV measurement plane. It is important to mention that, in this study, while upstream and side surfaces can be taken sufficiently far away the robot, the downstream surface (measurement plane) is rather close to the wings such that the previous hypothesis is not fully verified. That is, integration of pressure and turbulent stresses on the downstream surface would theoretically yield more accurate results. However, pressure and turbulence stresses are known to be strong sources of noise that can potentially affect forces estimation, in a more significant way than simply neglecting their integration.

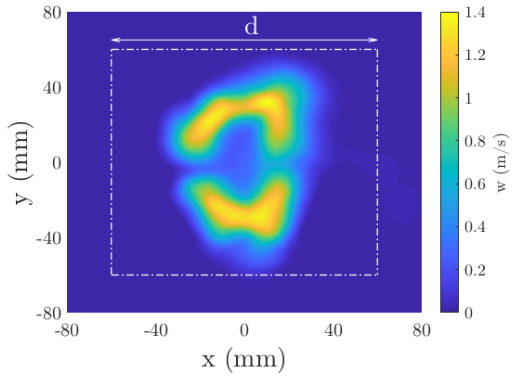

Figure 3: Contours of vertical velocity obtained from PIV measurements for wings operated at a frequency of 25 Hz and with an amplitude of 120°.

Figure 3 shows the magnitude of the vertical velocity component in the measurement plane for wings operated at a frequency of 25 Hz and with an amplitude of 120°. A square control surface centered on the center of the wake is used. Its boundaries are depicted in white. Time-averaged lift is deduced from integration of the vertical velocity field over this control surface. Figure 4 shows the time-averaged lift as a function of the charactestic dimension of the control surface, d. It is shown that the extent of the measurement plane is enough to ensure that lift is converged with respect to the size of the control surface (it staurates for $d > 100$mm), i.e. the side boundaries are sufficiently far away from the wake.

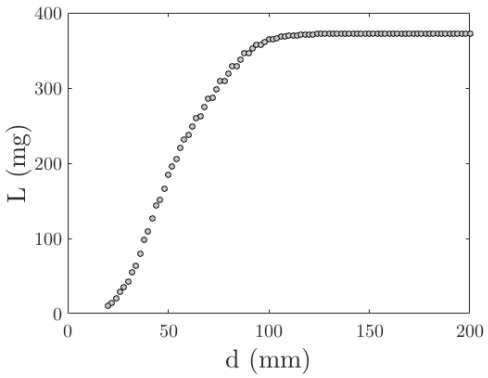

Figure 4: Lift as a function of the characteristic dimension of the control surface.

2.4 High-speed visualizations

A X-Stream Vision 3 IDT high speed camera (1080 px $\times$ 1024 px resolution) placed perpendicularly to the mean wing path (i.e. to the PIV measurement plane) acquires images of the wings at frequencies up to 600 Hz. Figure 5 shows a sequence obtained during one stroke of the flapping motion for wings operated at a frequency of 25 Hz and with an amplitude of 120°. Assuming that wing pitch motion is a solid rotation of the membrane around the hinge, one can estimate the instantaneous angle of attack of the wing, α, by measuring the projected wing chord onto the image, $c\cos\alpha$ (c being the wing chord). Furthermore, one can measure the effective flapping angle of the wing which is here taken as the angular displacement of the wing tip. It can be seen that because the wing bends spanwise, the effective flapping angle is larger than the flapping amplitude of the rod-crank system. It should be noticed that a stroke starts when the angle produced by the rod-crank system is maximum, which does not necessarily corresponds to maximum angle of attack and/or maximum effective flapping angle precisely because of fluid-structure interactions (passive pitch and spanwise bending). Two 150 W Dedolight Halogen light spots are used to continuously illuminate the wings and image acquisition is performed with an exposure time of 300 μs. Filters are then used to enhance the image contrast and extract the wing geometry.

Figure 6 displays the instantaneous angle of attack, α, and effective flapping angle, ϕ, as a function of time (non-

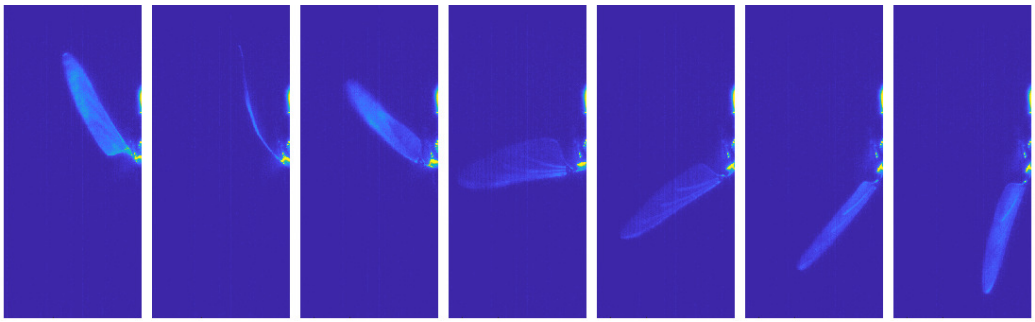

Figure 5: Visualizations of a single wing at 7 instants during one flapping stroke for flapping amplitude $\Delta\phi = 120°$ and frequency $f = 25$Hz.

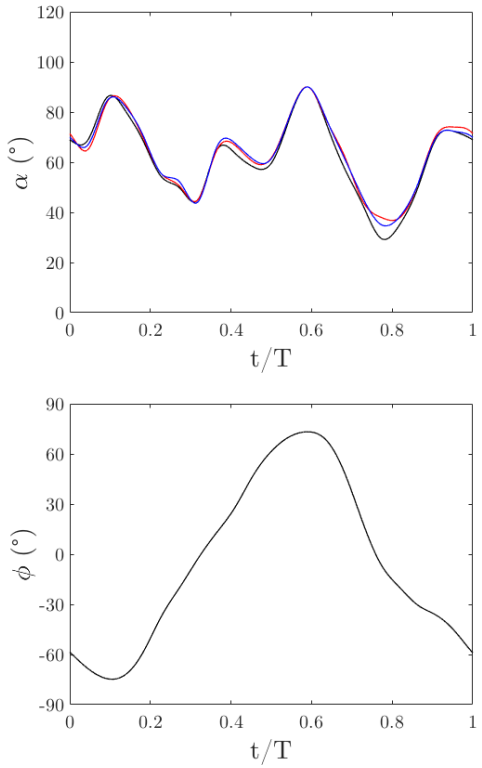

Figure 6: Instantaneous angle of attack and effective flapping angle as a function of non-dimensional time, extracted from HSV for flapping amplitude $\Delta\phi = 120°$ and frequency $f = 25$Hz. α is shown for three consecutive flapping cycles.

dimensionalized by the flapping period T), for three consecutive flapping cycles. Kinematics are shown for the case considered in figure 5. It can be seen that the signal is reasonably repeatable from one cycle to another. In addition, as previously explained, it can already be noticed that the angle of attack does not pass through 90° at $t/T = 0$, i.e. passive pitch induces a phase-lag with stroke reversal. Similarly, the effective flapping angle is not maximum at $t/T = 0$ because of spanwise bending.

2.5 *Direct numerical simulations*

Instantaneous angle of attack and flapping angle are then implemented in a code that directly solves the incompressible form of the Navier-Stokes equations on a finite volume mesh enclosing one wing. An overset grid approach is used that allows the wing mesh to move following prescribed flapping and pitching motions within a stationnary background mesh. The trimmed mesh consists of 5 million hexahedral cells (2.25 million for wing mesh and 2.75 million for background mesh) enclosed within a cylindrical domain of radius 30R and height 40R. The typical cell size at the wing surface and in the close wake is equal to $c/100$ and $c/50$ respectively. The boundary conditions upstream and downstream of the wing are implemented as pressure Dirichlet conditions while the periphery of the cylindrical domain is defined using a slip-wall condition. The wing is modelled as a non-slip surface. Wing mesh is moved with a time step that is 400 times smaller than the flapping period. Both spatial and temporal discretizations are achieved using second-order schemes. Momentum and continuity equations are solved in an uncoupled manner using a predictor-corrector approach.

Preliminary tests showed that aerodynamic loads are converged with respect to both spatial and temporal discretizations. In addition, 10 periods were simulated to allow for initial transients to sufficiently decay.

3 RESULTS

3.1 *Mean lifting force*

Figure 7 shows the lift (in mg) generated by wings flapping with frequencies up to 30 Hz and flapping amplitudes 60, 90 and 120°.

First, it can be observed that reasonable agreement (within the error bar) is achieved between loads obtained from balance and PIV measurements. In addition to cross-validating both approaches, this indicates that load estimation from PIV measurements can be used for non-intrusive measurements and suggests that the approach could be suited to even weaker magnitudes of lift (e.g. smaller robot dimensions) for which typical balance ranges are not adapted. Lift obtained from DNS overestimates by 12.6% experimental values. This overestimation may partly arise from the solid rotation asumption (the numerical simulation does not account for spanwise wing deformation), inaccuracy in kinematics extraction from HSV and in the fact that only one wing is being simulated.

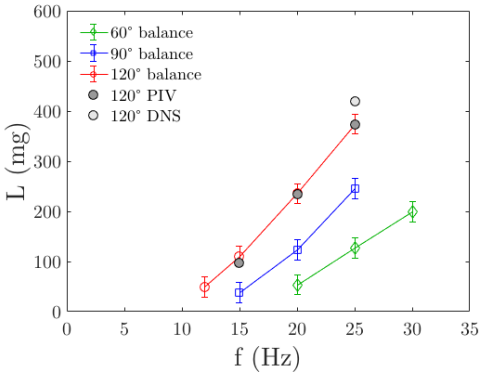

Figure 7: Lift force generated by the flapping wings as a function of the flapping frequency f for three amplitudes $\Delta\phi = 60, 90$ and 120°. Comparison between results obtained experimentally (balance and PIV) and numerically (DNS).

Second, it can be observed that constant-amplitude lift curves do not approach pure quadratic functions of the frequency. For prescribed angles of attack, a first approximation is to consider a constant lift coefficient C_L such that lift is a quadratic function of both flapping amplitude and frequency $L = \frac{1}{2}\rho A C_L (2\Delta\phi R f)^2$, where ρ is the fluid density, $\Delta\phi$ is the flapping angle swept by the wing and A and R are the wings area and radius respectively. This relationship helps explain the observed increase in lift with both amplitude and frequency but does not allow for the observed lift-to-frequency relationship (alternatively lift-to-amplitude relationship) to be predicted. Here, passive pitch due to fluid-structure interactions imply that the instantaneous angle of attack of the wing highly depends on both flapping amplitudes and frequencies. In particular, operating frequencies lower than 10 Hz did not allow for sufficient pitch motion such that no lift was generated, whatever the flapping amplitude.

Figure 8 shows the lift generated under similar operating conditions but with a thicker, 50 μm thick hinge. Again, reasonable agreement is observed between direct balance measurements and PIV measurements, which supports previous conclusions. Furthermore, it is observed that no significant differences exist with results obtained with a 25 μm thick hinge. In other words, effects of hinge flexibility on fluid-structure interaction processes appears to be of second order as compared to aerodynamic forces and wing weight and inertia.

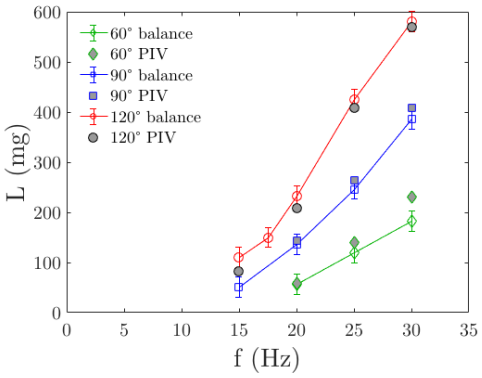

Figure 8: Lift force generated by the flapping wings as a function of the flapping frequency f for three amplitudes $\Delta\phi = 60$, 90 and 120°. Results obtained experimentally (balance and PIV) with a 50 μm thick hinge.

Overall, it is demonstrated that the robot can generate enough lift force (i.e. superior to its weight) for sufficiently large flapping amplitude and frequency, typically $\Delta\phi > 90°$ and $f > 20$ Hz. Lift up to nearly three times the target weight is obtained for $\Delta\phi = 120°$ and $f = 30$ Hz.

3.2 *Passive pitch*

The effect of frequency and amplitude on passive pitch motion is highlighted on figure 9 which shows the instantaneous angle of attack α (phase-averaged over 2 consecutive strokes) extracted from high-speed visualizations. α is here measured with respect to the wing path direction. Three cases with $\Delta\phi = 120°$, $f = 25$ Hz; $\Delta\phi = 120°$, $f = 15$ Hz and $\Delta\phi = 60°$, $f = 25$ Hz are compared. It is observed that the wing operates at relatively similar angles of attack for $\Delta\phi = 120°$, $f = 15$ Hz and $\Delta\phi = 60°$, $f = 25$ Hz explaining comparable values of averaged lift for these two cases (see figure 8). Conversely, the wing operates at lower angle of attack in the $\Delta\phi = 120°$, $f = 25$ Hz case, which explains a larger production of lift for this case. Mean values of α are 66, 76 and 77° for cases $\Delta\phi = 120°$, $f = 25$ Hz; $\Delta\phi = 120°$, $f = 15$ Hz and $\Delta\phi = 60°$, $f = 25$ Hz, respectively.

In addition, it is shown that all α curves exhibit a complex trend with multiple harmonics. These complex trends, together with a limited passive pitch motion (which does not allow for sufficiently low, sustained values of α to be obtained over one stroke), are not optimal in terms of aerodynamic performance. Thus, although sufficient lifting force is provided, further improvements can be achieved through modifications of the wing structure to promote passive pitch motion.

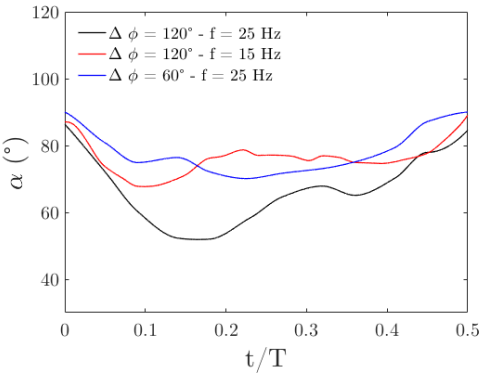

Figure 9: Comparison of instantaneous angles of attack extracted from HSV for cases with $\Delta\phi = 120°$, frequency $f = 25$Hz; $\Delta\phi = 120°$, frequency $f = 15$Hz and $\Delta\phi = 60°$, frequency $f = 25$Hz.

3.3 Correlation between instantaneous lift and flow physics

Wing kinematics extracted from high-speed visualizations (figure 6) are implemented in a flow solver to predict the instantaneous force generated by a single wing (with 25μm thick hinge) flapping at a frequency of 25 Hz and with an amplitude of 120°.

Figure 10 displays the instaneous lift generated by the wing over a flapping period. The curve exhibits low levels of lift around $t/T = 0$, 0.5 and 1, i.e. at stroke reversal where the wing velocity approaches zero. Immediatly after stroke reversal, two lift peaks ($t/T \approx 0.15$ and $t/T \approx 0.65$) are generated despite the relatively high angle of attack (figure 6). These peaks most presumably result from strong added mass effects associated with the severe acceleration of the wing. It was observed from figure 5 that the wing bends along its span as it changes direction, and then strongly accelerates as a response to internal stresses. Note that while wing bending is not directly taken into account in the numerical simulation, the resulting acceleration is intrinsically contained in the wing kinematics implemented in the flow solver. After these peaks, the angle of attack decreases to values that favor lift production (approximately 45 and 30° in the first and second halft stroke respectively) through the generation of a leading edge vortex.

Figure 11 shows iso-surfaces of Q-criterion during one stroke. Overall, the flow is characterized by multiple small

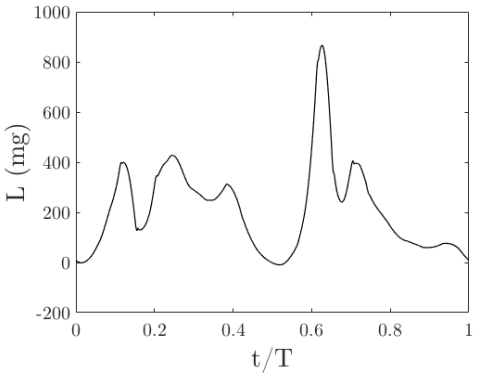

Figure 10: Instantaneous lift obtained numerically for wings operated with flapping amplitude $\Delta\phi = 120°$ and frequency $f = 25$Hz.

scale structures on the outboard portion and in the wake of the wing. These structures strongly interact with the wing at stroke reversal (first and second snapshots). As the wing further revolves about its root, a leading edge vortex (LEV) is formed, which exhibits a dual shape structure [6] (third snapshot). The LEV, a principal contributor to lift generation on flapping and revolving wings [7], develops from the root to a radial station where it bursts into small scale structures. In the inboard region, the LEV appears to remain attached to the wing for the whole stroke. It eventually lifts off the wing surface at the next stroke reversal (last snapshot).

As such, DNS shows that despite the chaotic trend and the relatively high value of angle of attack during one stroke, a relatively stable LEV develops on the wing, which favors lift production. In addition, spanwise bending induces strong acceleration at stroke reversal, which also contributes to lift generation through large-amplitude lift peaks.

4 Conclusion

We reported on the development of a 200 mg, bio-inspired nano flying robot. We addressed the main issues related to the development of extremely small-sized and light-weight vehicles in terms of manufacturing materials and processes as well as performance evaluation. Using direct balance measurement and indirect lift evaluation by particle image velocimetry, we showed that the robot was able to generate lift about three times its weight when the wings were operated at the largest frequency and amplitude tested. In addition, we provided insight into the instantaneous generation of lift by measuring the wing kinematics (with passive pitch motion) and implemented them in a flow solver, which further gives access to the full three-dimensional flow field around the wings. It was suggested that although the wings were able to generate a sustained LEV throughout the stroke and could benefit from spanwise bending at stroke reversal to produce lift, further imporvements could be achieved in terms of

aerodynamic performance through modification of the wing structure and enhanced passive pitch motion.

Acknowledgements

The authors would like to thank DGA (Délégation Générale de l'Armement) for funding this work under the 'Libellule' III project.

References

[1] D. Floreano and R. Wood. Science, technology and the future of small autonomous drones. *Nature*, 521(7553):460, 2015.

[2] E.W. Hawkes and D. Lentink. Fruit fly scale robots can hover longer with flapping wings than with spinning wings. *Journal of the Royal Society Interface*, 13(123):20160730, 2016.

[3] D.F. Kurtulus, F. Scarano, and L. David. Unsteady aerodynamic forces estimation on a square cylinder by tr-piv. *Experiments in Fluids*, 42(2):185–196, 2007.

[4] L. David, T. Jardin, and A. Farcy. On the non-intrusive evaluation of fluid forces with the momentum equation approach. *Measurement Science and Technology*, 20(9):095401, 2009.

[5] B.W. van Oudheusden, F. Scarano, E.W. Roosenboom, E.W. Casimiri, and L.J. Souverein. Evaluation of integral forces and pressure fields from planar velocimetry data for incompressible and compressible flows. *Experiments in Fluids*, 43(2-3):153–162, 2007.

[6] Y. Lu, G.X. Shen, and G.J. Lai. Dual leading-edge vortices on flapping wings. *Journal of Experimental Biology*, 209(24):5005–5016, 2006.

[7] M.H. Dickinson, F.O. Lehmann, and S.P. Sane. Wing rotation and the aerodynamic basis of insect flight. *Science*, 284(5422):1954–1960, 1999.

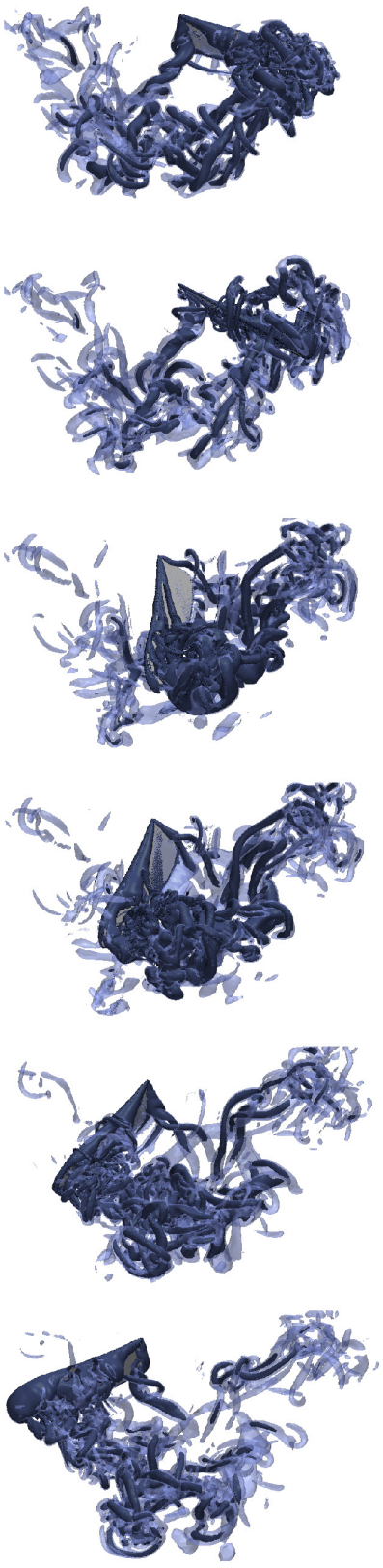

Figure 11: Sequence of Q-criterion isosurfaces obtained from DNS for flapping amplitude $\Delta\phi = 120°$ and frequency $f = 25$Hz.